PREDICTION OF A HEAT TRANSFER TO CO_2 FLOWING IN AN UPWARD PATH AT A SUPERCRITICAL PRESSURE

BONG-HYUN CHO*, YOUNG-IN KIM and YOON-YEONG BAE
Korea Atomic Energy Research Institute
1045 Daedeokdaero, Yuseong, Daejeon 305-353, Korea
*Corresponding author. E-mail : bhcho1@kaeri.re.kr

Invited March 28, 2008
Received October 30, 2008

This study was performed to evaluate the prediction capability of a commercial CFD code and to investigate the effects of different geometries such as a 4.4 mm tube and an 8/10 mm annular channel on the detailed flow structures. A numerical simulation was performed for the conditions, at which the experimental data was produced by the test facility SPHINX. A 2-dimensional axi-symmetric steady flow was assumed for computational simplicity. The RNG k-ε turbulence model (RNG) with an enhanced wall treatment option, SST k-ω (SST) and low Reynolds Abid turbulence model (ABD) were employed and the numerical predictions were compared with the experimental data generated from the experiment. The effects of the geometry on heat transfer were investigated. The flow and temperature fields were also examined in order to investigate the mechanism of heat transfer near the wall. The local heat transfer coefficient predicted by the RNG model is very close to the measurement result for the tube. In contrast, the local heat transfer coefficient predicted by the SST and ABD models is closer to the measurement for the annular channel.

KEYWORDS : Convective Heat Transfer, Supercritical Pressure, Upward Path, CO_2, CFD, Tube, Annular Channel

1. INTRODUCTION

An accurate prediction of the heat transfer coefficient for a water coolant at a supercritical pressure is very important for the design of a Supercritical Water Cooled Reactor (SCWR). The current study focuses on this critical issue of measuring heat transfer to supercritical water at prototypical SCWR conditions and evaluating the computational tools for the prediction of the SCWR thermal behaviors. For these purposes, the heat transfer test loop SPHINX using a surrogate fluid of CO_2 has been constructed at the KAERI. The experiment covers a study of the heat transfer characteristics in a single tube and a single rod at supercritical pressure conditions [1,2]. A numerical simulation of the flow and thermal fields using the commercial CFD code Fluent was performed to support these experiments by providing pre-test calculations and to investigate the effects of different geometries such as a 4.4 mm tube and an 8/10 mm annular channel on the detailed flow structures. To the best of the authors' knowledge, the effect of the geometry on a supercritical heat transfer has not been seriously examined. In the SCWR core, the sub-channels are much narrower than those of a conventional PWR, and accurate knowledge of a heat transfer in a narrow channel is necessary for a reliable design of a SCWR core. The previous numerical study by Kim et al. [3] showed that at a supercritical pressure the RNG turbulence model (RNG) with an enhanced wall treatment option reproduces the experimental results better than the wall function models. In this study the prediction capability of the RNG model with an enhanced wall treatment is compared with the SST k-ω model (SST) and one of the low-Reynolds number models (ABD). A steady state, incompressible flow and 2D axi-symmetric computational domain were assumed for computational simplicity. Three turbulence models were evaluated by comparing their predictions with the experimental results.

In previous studies, the complex heat transfer phenomena at supercritical conditions were explained by the substantial variations of the physical properties (density, thermal conductivity, viscosity, and heat capacity) with the temperature near the wall. The buoyancy and thermal acceleration due to a sudden decrease of the density near the wall modifies the radial shear stress distribution across a flow, and consequently inhibits a heat transfer as well [4,5]. The experimental data for the flow field near a wall at supercritical conditions are not available due to the difficulties in the measurement at a high pressure. In this study, the flow and temperature fields will be examined in detail numerically in order to analyze the mechanism of a heat transfer near the wall. The numerical simulations are expected to provide us with meaningful information on the heat transfer behaviors at supercritical conditions with much less cost than an experimental campaign .

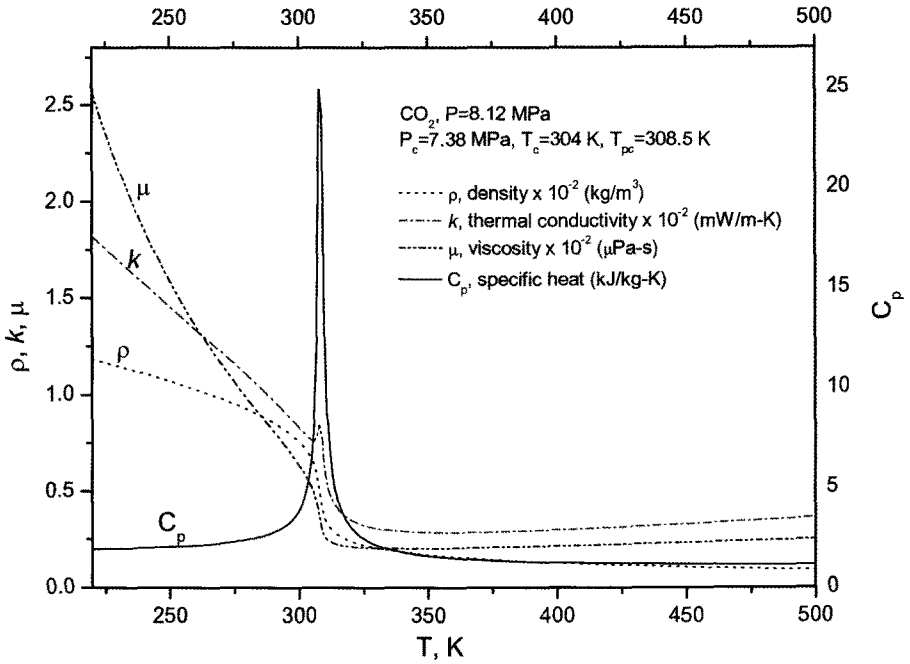

c: critical; pc: pseudo-critical

Fig. 1. Physical properties of CO_2 at a supercritical pressure

2. NUMERICAL METHOD

2.1 Physical Properties

The variations of physical properties of CO_2 at a supercritical pressure (P=8.12 MPa, P/P_c=1.1) are shown in Fig. 1. The specific heat shows a distinct spike at around the pseudo-critical temperature, and the other fluid properties such as the thermal conductivity, density, viscosity, and enthalpy vary rapidly near the pseudo-critical temperature (T_{pc}=308.5 K). At a supercritical pressure, a rapid change of the fluid properties with the temperature influences the heat transfer phenomena, therefore accurate inputs for the fluid properties are very important for a heat transfer calculation. The NIST Standard Reference Database 23(REFPROP) Version 7 [6] was used to obtain the required fluid properties. This property data has been incorporated into the Fluent code as a user defined function in these calculations.

2.2 Mean Flow Equations

For a steady state incompressible flow in two-dimensional (2D) cylindrical coordinates, the mean flow conservation equations for the axial and radial directions are described as follows:

Continuity

$$\frac{1}{r}\left[\frac{\partial}{\partial x}(r\rho U)+\frac{\partial}{\partial r}(r\rho V)\right]=0 \tag{1}$$

U-momentum

$$\frac{1}{r}\left[\frac{\partial}{\partial x}(r\rho U^2)+\frac{\partial}{\partial r}(r\rho UV)\right] = -\frac{\partial P}{\partial x}+\frac{1}{r}\left\{2\frac{\partial}{\partial x}\left[r(\mu+\mu_t)\frac{\partial U}{\partial x}\right]+\frac{\partial}{\partial r}\left[r(\mu+\mu_t)\left(\frac{\partial V}{\partial x}+\frac{\partial U}{\partial r}\right)\right]\right\}-\rho g \tag{2}$$

V-momentum

$$\frac{1}{r}\left[\frac{\partial}{\partial x}(r\rho VU)+\frac{\partial}{\partial r}(r\rho V^2)\right] = -\frac{\partial P}{\partial r}+\frac{1}{r}\left\{\frac{\partial}{\partial x}\left[r(\mu+\mu_t)\left(\frac{\partial V}{\partial x}+\frac{\partial U}{\partial r}\right)\right]+2\frac{\partial}{\partial r}\left[r(\mu+\mu_t)\frac{\partial V}{\partial r}\right]\right\}-2\frac{(\mu+\mu_t)V}{r^2} \tag{3}$$

where μ_t is the eddy viscosity and ρ is the density. The buoyancy effect is included in the momentum equation.

The energy equation for the case where there are variations of properties with a temperature is:

Energy (temperature)

$$\frac{\partial}{\partial x}(\rho C_p UT)+\frac{1}{r}\frac{\partial}{\partial r}(r\rho C_p VT) = \frac{1}{r}\left\{\frac{\partial}{\partial x}\left[rC_p\left(\frac{\mu}{\mathrm{Pr}}+\frac{\mu_t}{\mathrm{Pr}_t}\right)\frac{\partial T}{\partial x}\right]+\frac{\partial}{\partial r}\left[rC_p\left(\frac{\mu}{\mathrm{Pr}}+\frac{\mu_t}{\mathrm{Pr}_t}\right)\frac{\partial T}{\partial r}\right]\right\} \tag{4}$$

where, Pr is the molecular Prandtl number and Pr_t is the turbulent Prandtl number.

2.3 Turbulence Models and Equations

The selected turbulence models for these predictions are the Re-Normalization Group k-ε (RNG) [7], the Shear-Stress Transport k-ω (SST) [8], and the Abid (ABD) [9] model. The last model is selected for this study because it is one of the candidates among the low-Reynolds k-ε models. The RNG model is known to provide better results than the standard k-ε model for a flow field with rapid strain rates and streamline curvatures. In this model the turbulent Prandtl number is calculated by an analytical formula rather than a constant. The scale elimination procedure in the RNG theory also provides an analytically-derived differential formula for an effective viscosity that allows the model to handle a low-Reynolds-number and near-wall flows better [10]. The SST model blends the robust and accurate formulation of the k-ω model in the near-wall region with the free-stream dependency of the k-ε model in the far field. The low-Reynolds k-ε model is able to modify the standard k-ε model by using some complex damping functions for the ε–transport equation and eddy viscosity, which permits an integration of the turbulence transport equations over a viscous sub-layer. Damping functions are written in terms of the turbulent Reynolds number.

The governing turbulence model equations are as follows:

(1) Eddy viscosity modeling

$$\mu_t = C_\mu f_\mu \frac{\rho k^2}{\varepsilon} \quad \text{(for the } k\text{-}\varepsilon \text{ model)}$$

$$\mu_t = \frac{\rho k}{\omega} \frac{1}{\max\left[\frac{1}{\alpha^*}, \frac{SF_2}{\alpha_{1\varpi}}\right]} \quad \text{(for the } k\text{-}\omega \text{ model)} \tag{5}$$

In the k-ω model, the coefficient α^* damps the eddy viscosity causing a low-Reynolds number correction. S is the strain rate magnitude. The details of the coefficients and constants used in the above equation are defined in the Reference [10].

(2) k and ε-transport or ω-transport

$$\frac{\partial}{\partial x}(\rho U\Phi) + \frac{1}{r}\frac{\partial}{\partial r}(r\rho V\Phi) = \frac{\partial}{\partial x}(\Gamma_\Phi \frac{\partial \Phi}{\partial x}) + \frac{1}{r}\frac{\partial}{\partial r}(r\Gamma_\Phi \frac{\partial \Phi}{\partial r}) + S_\Phi \tag{6}$$

where Φ means the generalized dependent variable. Γ_Φ and S_Φ represent the effective diffusivity and source term for each dependent variables, respectively. The dependent variables, effective diffusivities and source terms per each turbulence model are defined in Table 1.

The RNG model uses inverse effective Prandtl numbers, α_k and α_ε which are computed using the following formula derived analytically by the RNG theory.

$$\left|\frac{\alpha - 1.3929}{\alpha_0 - 1.3929}\right|^{0.6321} \left|\frac{\alpha + 2.3929}{\alpha_0 + 2.3929}\right|^{0.3679} = \frac{\mu_{mol}}{\mu_{eff}} \tag{7}$$

In the SST model, σ_k and σ_ω are the turbulent Prandtl numbers for k and ω, respectively and defined as follows.

$$\sigma_k = \frac{1}{F_1/\sigma_{k1} + (1-F_1)/\sigma_{k2}} \tag{8}$$

$$\sigma_\varpi = \frac{1}{F_1/\sigma_{\varpi 1} + (1-F_1)/\sigma_{\varpi 2}} \tag{9}$$

The blending functions F_1 and F_2 are described in detail in the Reference [8,10].

Table 1. Dependent Variables, Effective Diffusivities and Source Terms of the Turbulence Models

Turbulence Model	Φ	Γ_Φ	S_Φ
RNG	k	$\alpha_k(\mu + \mu_t)$	$G_k + G_b - \rho\varepsilon$
	ε	$\alpha_\varepsilon(\mu + \mu_t)$	$C_{\varepsilon 1}\frac{\varepsilon}{k}G_k - C_{\varepsilon 2}\rho\frac{\varepsilon^2}{k} - R_\varepsilon$
SST	k	$(\mu + \mu_t/\sigma_k)$	$G_k - Y_k + S_k$
	ω	$(\mu + \mu_t/\sigma_\omega)$	$G_\omega - Y_\omega + S_\omega + D_\omega$
ABD	k	$(\mu + \mu_t/\sigma_k)$	$G_k + G_b - \rho\varepsilon + S_k$
	$\tilde{\varepsilon}$	$(\mu + \mu_t/\sigma_\varepsilon)$	$f_1 C_{\varepsilon 1}\frac{\varepsilon}{k}(G_k - C_{\varepsilon 3}G_b) - f_2 C_{\varepsilon 2}\rho\frac{\varepsilon^2}{k} + S_\varepsilon$

Among the source terms in Table 1, G_k represents the generation of the turbulent kinetic energy due to the mean velocity gradients. G_b is the generation of the turbulent kinetic energy due to a buoyancy effect. G_ω is the generation of ω. Y_k and Y_ω are the dissipation of k and ω due to a turbulence. S_k, S_ε, and S_ω are user defined source terms. D_ω is the cross-diffusion term.

The damping function used for the ABD model is as follows;

$$f_\mu = \tanh\left(0.008\,\mathrm{Re}_y\right)\left(1+4\,\mathrm{Re}_t^{-3/4}\right);\ f_1 = 1;\ \mathrm{Re}_t = \frac{k^2}{\nu\tilde{\varepsilon}};\ \mathrm{Re}_y = \frac{\sqrt{k}\,y}{\nu};$$
$$f_2 = \left[1-\frac{2}{9}\exp\left(-\frac{\mathrm{Re}_t^{\,2}}{36}\right)\right]\left[1-\exp\left(-\frac{\mathrm{Re}_t}{12}\right)\right]^2 \quad (10)$$

Here $\tilde{\varepsilon}$ is the modified dissipation variable to which the boundary condition $\tilde{\varepsilon} = 0$ at $y = 0$ applies.

(3) Other model constants

The constants for the turbulence models are summarized in Table 2.

2.4 Wall Treatments

The two-layer approach in the Fluent code is an integral part of its enhanced wall treatment option and it is used to specify both ε and the eddy viscosity in near-wall cells. In this approach, the whole domain is subdivided into a viscosity-affected region and a fully-turbulent region, which are determined by the wall-distance-based, turbulent Reynolds number ($\mathrm{Re}_y \equiv \rho y\sqrt{k}/\mu$). In the fully-turbulent region ($Re_y > 200$), the high-Reynolds turbulence models are employed, while in the viscosity-affected region ($Re_y < 200$), one equation model of Wolfstein [11] is employed. The momentum equations and the k-equation are retained but the eddy viscosity is computed by equation (11) [12].

$$\mu_{t,2layer} = \rho C_\mu \ell_\mu \sqrt{k},\ \ \ell_\mu : \text{length scale} \quad (11)$$

In the enhanced wall treatment option, the eddy viscosity is smoothly blended with the high-Reynolds-number definition from the outer region, as proposed by Jongen [13].

$$\mu_{t,enh} = \lambda_\varepsilon \mu_t + (1-\lambda_\varepsilon)\mu_{t,2layer} \quad (12)$$

The blending function λ_ε is defined in such a way that it is equal to unity far from the walls and is zero very near to the walls. If the near-wall mesh is fine enough to be able to solve the laminar sub-layer (typically $y^+ \approx 1$), then the enhanced wall treatment option will be identical to a two layer zonal model.

Since the k-ω and low-Reynolds turbulence models require that the first grid off the wall has a height of $y_1^+ < 1$, these models have a fine grid near the wall. In our numerical simulation, one identical grid is used which has the nearest grid sufficiently fine enough everywhere at $y_1^+ < 1$ for all the models, and a two layer zonal model is used for all simulated cases.

2.5 Reference Experiments, Geometries, Flow, and Boundary Conditions

Among the SPHINX experiments, two cases are selected for comparison. The first test case is an Inconel 625 tube of 4.4 mm ID, which is vertically mounted in-between two connecting flanges. The tube is directly heated by DC power and the heated length is about 2,100 mm. The outer surface temperature of the tube is measured by 41 K-type thermocouples installed with an equal spacing of 50 mm. The other test case is a uniformly heated vertical annular channel between an 8 mm OD heater rod and a 10 mm ID tube. The heater rod (OD 8 mm, length 1.8 m) is indirectly heated by AC power. On the heater rod 12 thermocouples are spirally installed with a 60 degree phase difference. The first thermocouple is located 50 mm above the lower end of the heated section, and the successive 5 thermocouples are installed with an equal spacing of 100 mm above the first one. The remaining 6 thermocouples are located with an equal spacing of 200 mm above the lower 6 thermocouples. In order to obtain a fully developed flow field in the upstream and downstream of the heated region, both cases have an additional length of unheated parts. The details

Table 2. Constants of the Turbulence Models

Turbulence Model	C_μ	$C_{\varepsilon 1}$	$C_{\varepsilon 2}$	α_k or σ_k	α_ε, σ_ε or σ_ω
RNG	0.0845	1.42	1.68	$\alpha_k = 1.393$	$\alpha_\varepsilon = 1.393$
SST	-	-	-	$\sigma_{k1} = 1.176$ $\sigma_{k2} = 1.0$	$\sigma_{\omega 1} = 2.0$ $\sigma_{\omega 2} = 1.168$
ABD	0.09	1.45	1.83	$\sigma_k = 1.0$	$\sigma_\varepsilon = 1.0$

CO_2, P=8.12MPa,
vertically upward flow
(a)4.4 mm Tube
(b) OD/ID (10/8 mm) Annulus

Heat flux [kW/m²]	Mass flux [kg/m²s]
50	1200
130	1200

*** Inlet Temp.: T_i=27.2℃ (300K)**

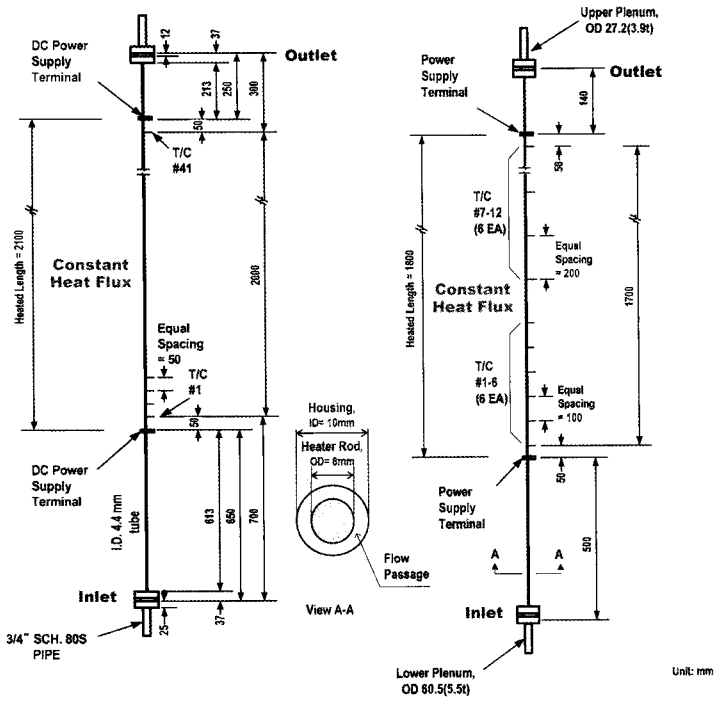

Fig. 2. Schematic of the Test Section (a) Tube; (b) Annular Channel

of the two test sections are shown in Fig. 2.

The mass flow rate for the 4.4 mm tube is determined so that the inlet *Re* number matches with the *Re* number at the core inlet of the prototype SCWR, which is about 50,000. The heat loading factor represents a normalized wall heat flux and appears as Equation (13) in the work by Jackson and Hall [14];

$$N_q = \frac{q'' D_{eq}}{k_b T_b} \text{ ; normalized wall heat flux} \qquad (13)$$

In order to have an equivalent heat loading factor, the equivalent diameter (D_{eq}) of the annular channel should be identical to the tube diameter. The equivalent hydraulic diameter of the annular channel is calculated based on the heated perimeter instead of the wetted perimeter. This results in the fact that the Reynolds number in the annular channel is about a half of that in the tube, when a same mass flux is applied. The equivalent hydraulic diameter of the annular channel is 4.5 mm when the heated perimeter concept is employed in the calculation. This is nearly identical to a tube with a 4.4 mm inner diameter, so the same mass and heat flux can be assigned for the tubes and annular channels for a similarity consideration. The SPHINX experiment confirmed that the heat transfer coefficient and Nusselt number for a tube and an annular channel showed a similar trend to each other and accordingly the scaling of the annular channel was considered a reasonable choice [15].

This numerical prediction covers the supercritical pressure CO_2 flowing upward in a uniformly heated vertical path with a mass flux of 1,200 kg/m²s and a wall heat flux range from 50 to 130 kW/m² at the supercritical pressure of 8.12 MPa. The inlet fluid temperature is assumed to be 300 K. We only deal with a steady state and 2D axi-symmetric flow field for computational simplicity. The computational domain includes all the flow fields between flanges. The inlet boundary condition is a constant velocity with a uniform temperature. The heated wall is defined as a constant heat flux and the unheated wall as an adiabatic wall.

3. RESULT AND DISCUSSION

3.1 Tube

The predicted wall temperatures and local heat transfer coefficients for the tube based on the RNG, SST, and ABD models are compared with the measurement results in Fig. 3. The heat flux varies from 50 to 130 kW/m² at a mass flux of 1,200 kg/m²s. We can see from Fig. 3 that the measurement results are in-between the predicted ones both by the RNG and SST models. At a heat flux of 50 kW/m², the local heat transfer coefficient predicted by the RNG model is very close to the measurement result

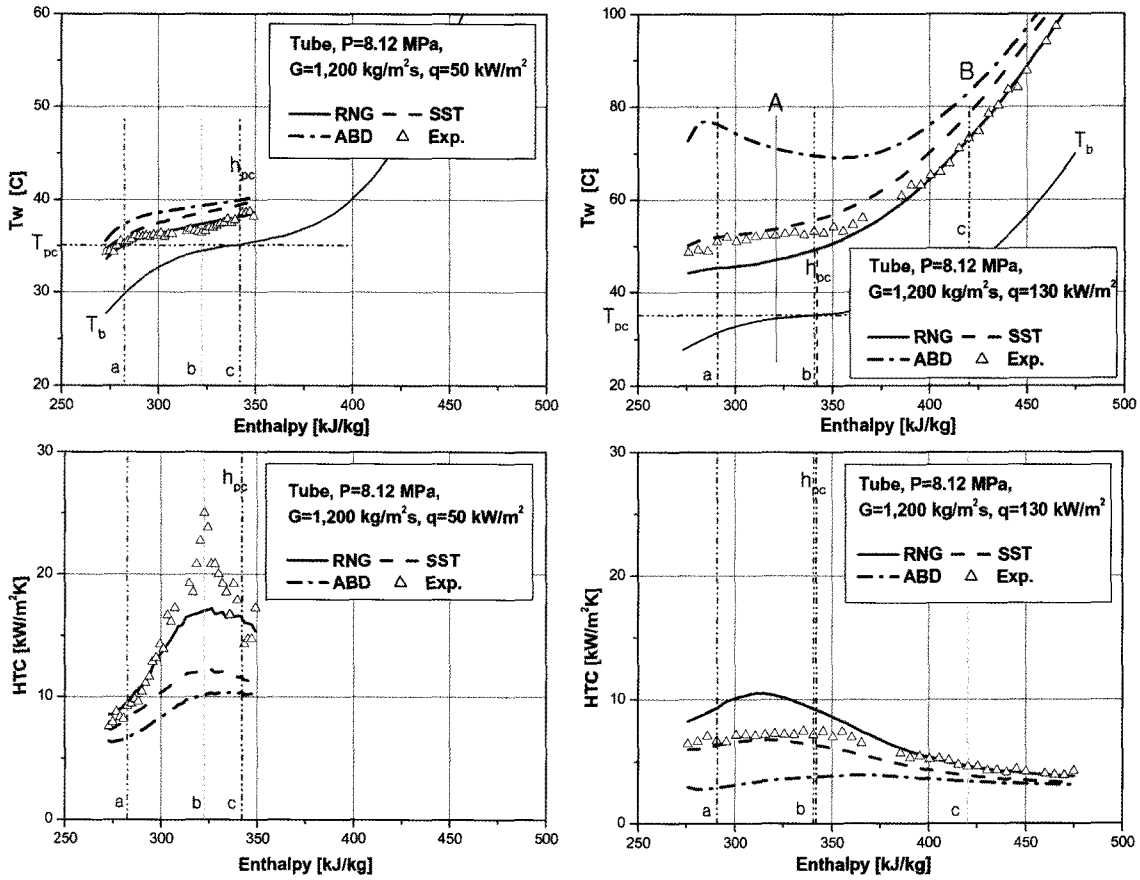

Fig. 3. Comparison of the Wall Temperature and Heat Transfer Coefficient for the 4.4 mm Tube

for the lower half of the tube length, where the bulk fluid temperature (T_b) is sufficiently lower than the pseudo-critical temperature (T_{pc}). Whereas, at a heat flux of 130 kW/m^2, the predicted local heat transfer coefficient is very close to the measurement result for the upper half of the tube length where $T_b >> T_{pc}$. When the T_b is slightly lower than the T_{pc} (or pseudo-critical enthalpy, h_{pc}), the heat transfer coefficient reaches a peak and this peak becomes lower with an increase of the heat flux. In this region a remarkable difference is seen in the heat transfer coefficient between the prediction and the measurement result. This difference can be explained by the fact that the experiment incorporates the real thermal transient at the inlet boundary but the prediction assumes the inlet boundary condition as a constant velocity with a uniform temperature. The ABD model shows a fairly large under-prediction of the heat transfer coefficient throughout the entire tube length due to an under-prediction of the turbulence near a wall, more so than the other two models did.

In order to examine the radial flow distribution at several axial locations, three reference cross-sections are selected as shown in Fig. 3 (a, b and c). Figs. 4-7 show the contour and the distribution of the temperature, specific heat, axial velocity, and density calculated by the two models for the cases of a heat flux of 50 and 130 kW/m^2, respectively.

In Fig. 4 the heated wall temperature reaches the pseudo-critical temperature first at location 'a,' about x=0.3 m downstream of the heated inlet, and the domain of the over-pseudo-critical temperature spreads to the center as the fluid flows downstream. The distribution of the specific heat (C_p) contour plot (RNG model) clearly shows this trend. Initially the higher region of the specific heat appears very close to the heated wall, and then it spreads throughout the flow in the downstream (location 'c,' where $T_b = T_{pc}$). When the fluid temperature approaches the pseudo-critical temperature, the fluid density experiences a drastic decrease and consequently the velocity starts to increase as shown in Fig. 5. At location 'c,' little difference is shown between the two models in the fluid temperature and axial velocity profiles but in the specific heat and density the differences are not negligible.

Figs. 6 and 7 show that the wall temperature changes from 316 K at the heated inlet to about 380 K at the outlet for the case of a heat flux of 130 kW/m^2. The wall temperature is already higher than the pseudo-critical

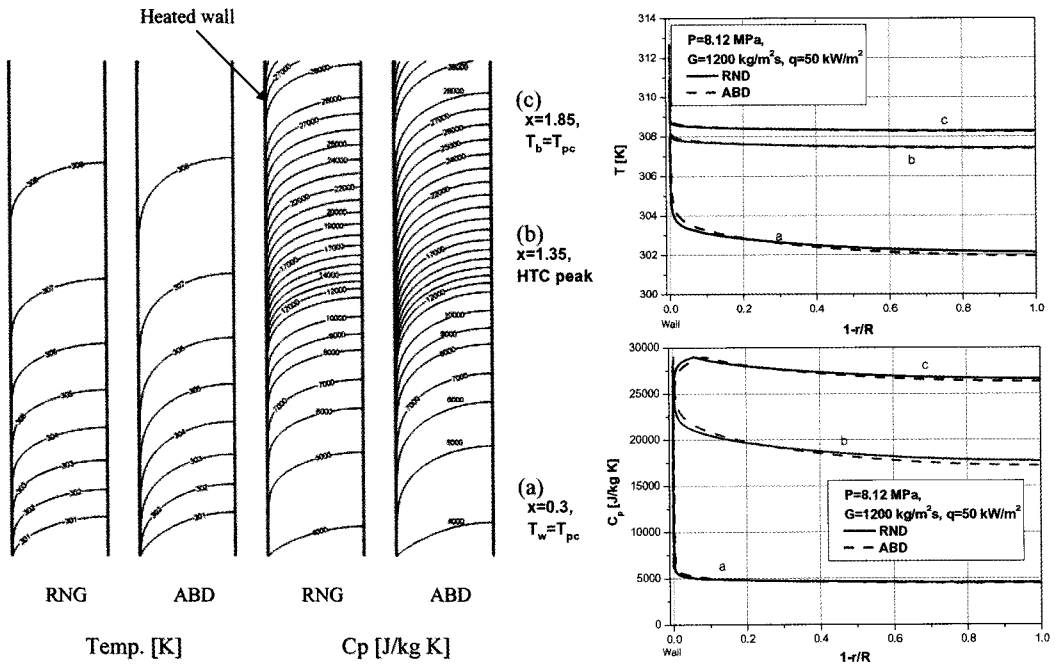

Fig. 4. Contour Plots and Comparison of the Predicted Temperature and Specific Heat Profiles at the Radial Coordinates for the 4.4 mm Tube (q=50 kW/m^2)

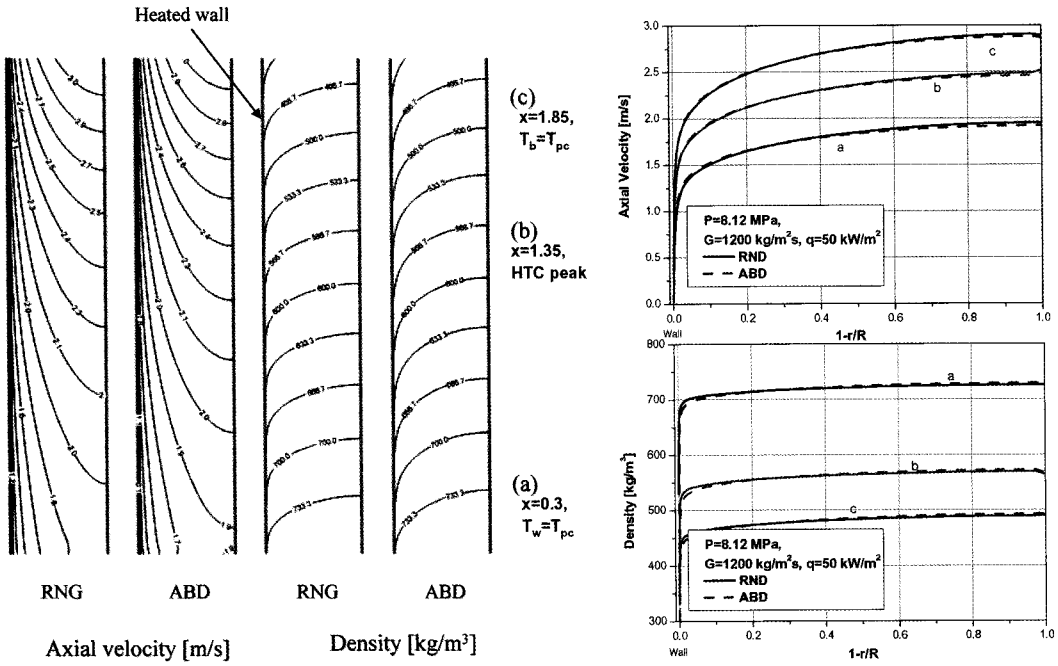

Fig. 5. Contour Plots and Comparison of the Predicted axial Velocity and Density Profiles at the Radial Coordinates for the 4.4 mm Tube (q=50 kW/m^2)

temperature from the starting point of the heated wall as shown in Fig. 6. At location 'b,' about x=0.7 m downstream of the heated inlet, the bulk fluid temperature reaches the pseudo-critical temperature first and the high specific heat region spreads into the entire cross section. These physical property profiles are very similar to those of the 50 kW/m^2 heat flux case, and the differences in the specific heat and density are more remarkable between the two

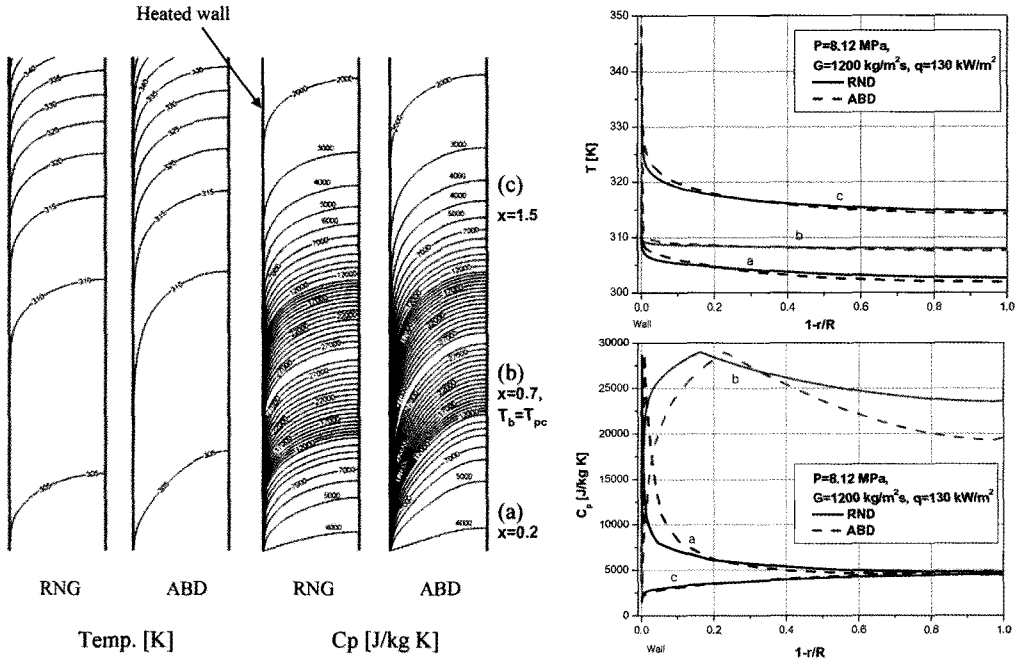

Fig. 6. Contour Plots and Comparison of the Predicted Temperature and Specific Heat Profiles at the Radial Coordinates for the 4.4 mm Tube (q=130 kW/m^2)

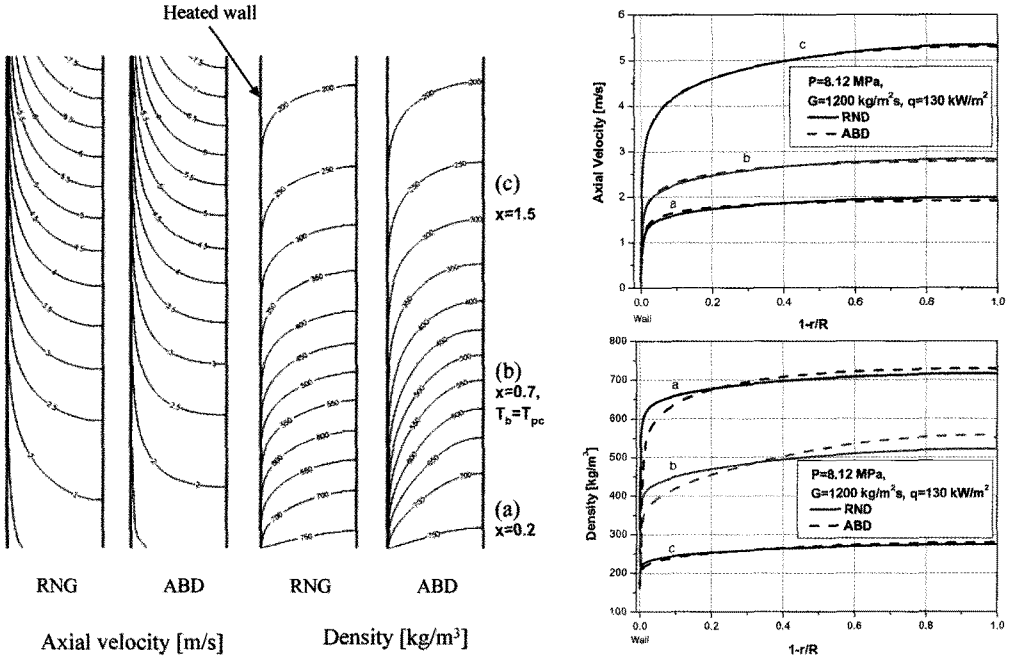

Fig. 7. Contour Plots and Comparison of the Predicted Axial Velocity and Density Profiles at the Radial Coordinates for the 4.4 mm Tube (q=130 kW/m^2)

models. After the specific heat reaches a peak at the cells very close to the heated wall for both cases the peak point moved toward the centerline until the bulk fluid temperature reaches its pseudo-critical temperature.

3.2 Annular Channel

The annular channel case has the same wall heat flux and mass flux as the corresponding case for the tube. Non-dimensional heat loading factors are used for a thermal

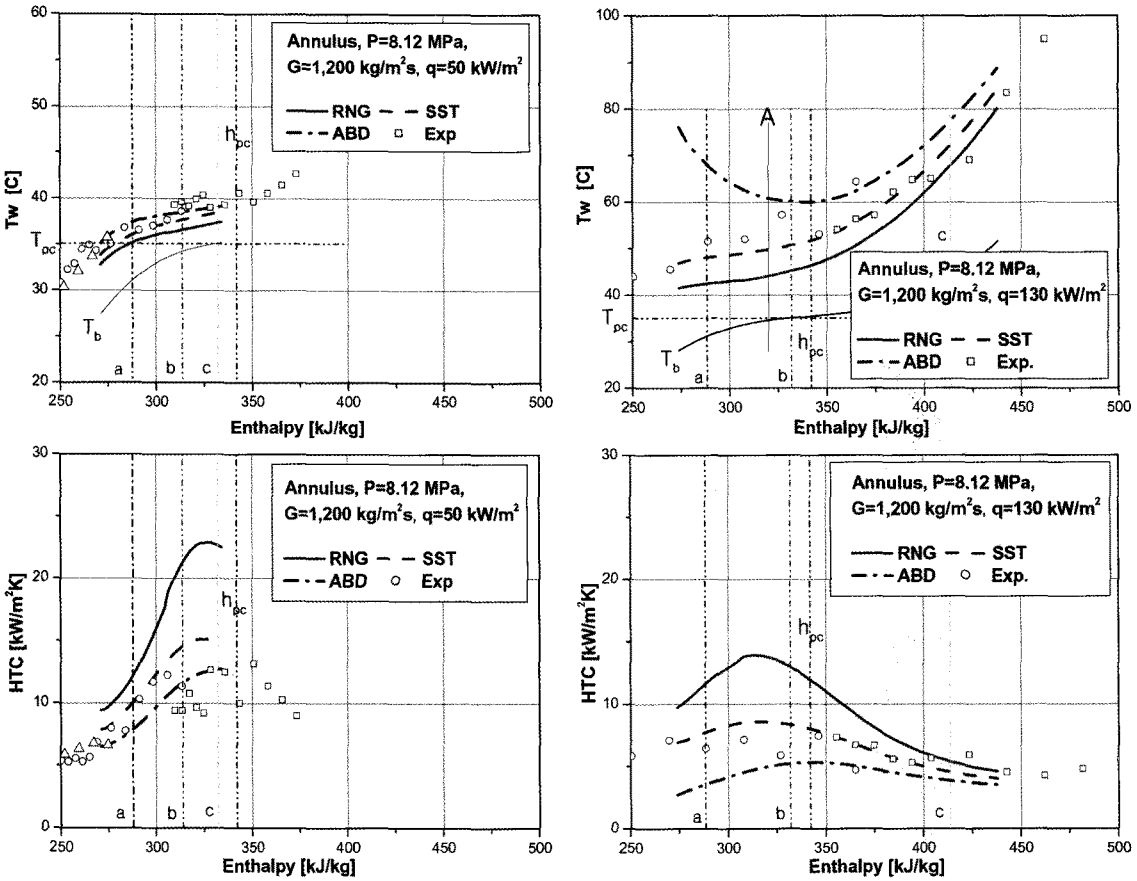

Fig. 8. Comparison of the Predicted Wall Temperature and Heat Transfer Coefficient for the 8/10 mm Annular Channel

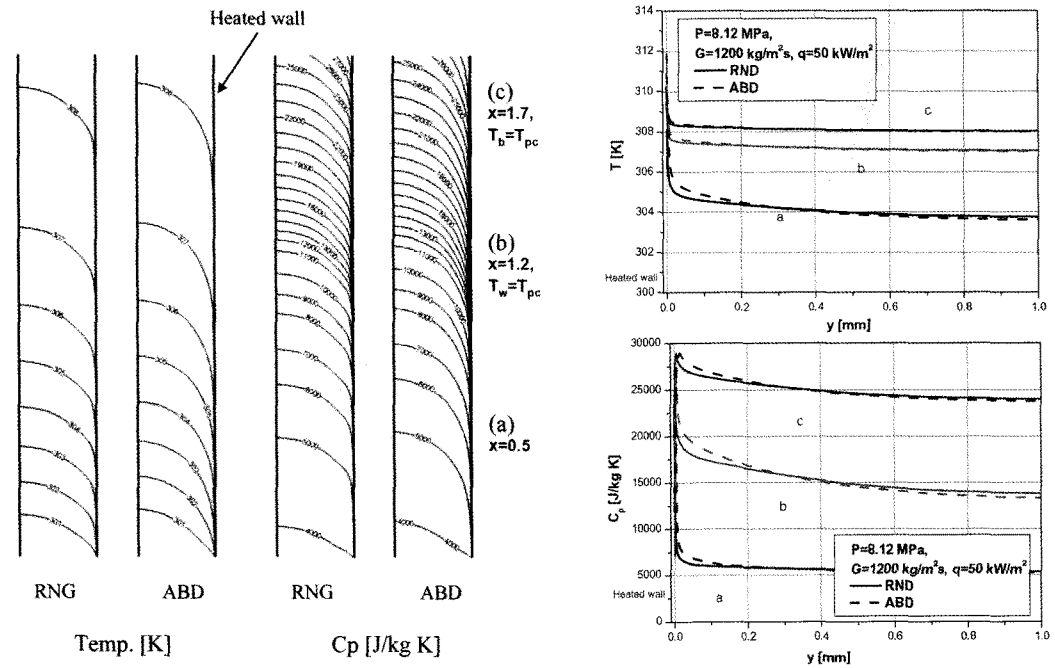

Fig. 9. Contour Plots and Comparison of the Predicted Temperature and Specific Heat Profiles at the Radial Coordinates for the 8/10 mm Annular Channel (q=50 kW/m^2)

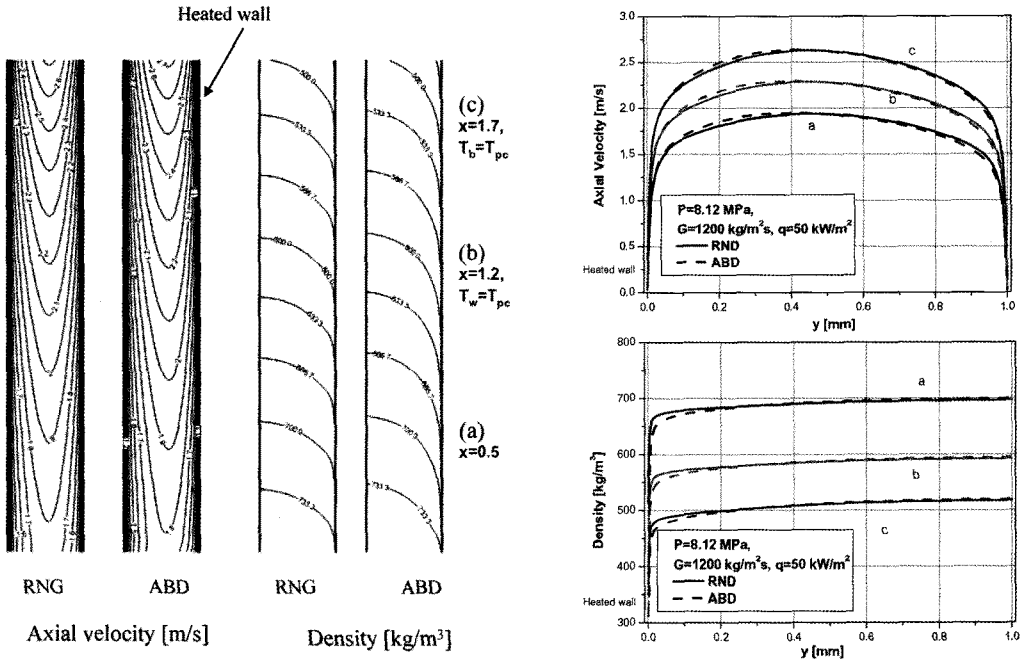

Fig. 10. Contour Plots and Comparison of the Predicted Axial Velocity and Density Profiles at the Radial Coordinates for the 8/10 mm Annular Channel (q=50 kW/m^2)

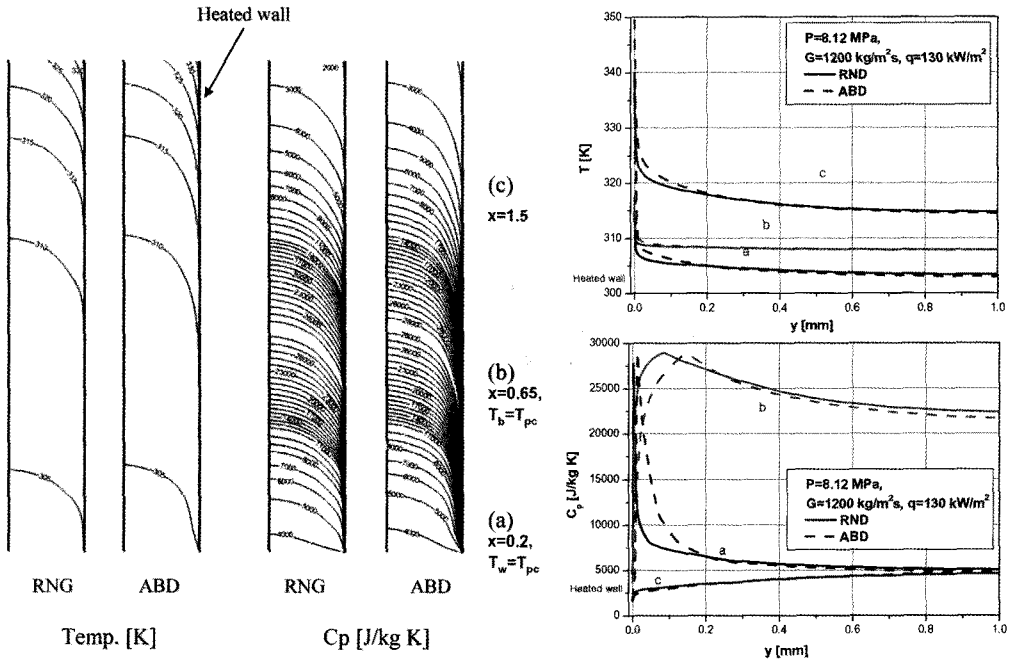

Fig. 11. Contour Plots and Comparison of the Predicted Temperature and Specific Heat Profiles at the Radial Coordinates for the 8/10 mm Annular Channel (q=130 kW/m^2)

similarity. The predicted wall temperatures for the annular channel based on the RNG, SST and ABD models are compared with the measurement result in Fig. 8. The heat flux also varies from 50 to 130 kW/m^2 at a mass flux of 1,200 kg/m^{2}s. Unlike the tube case, the local heat transfer coefficient predicted by the SST and ABD models is closer to the measurement result. When the T_b is slightly lower than the T_{pc}, the heat transfer coefficient reaches its peak

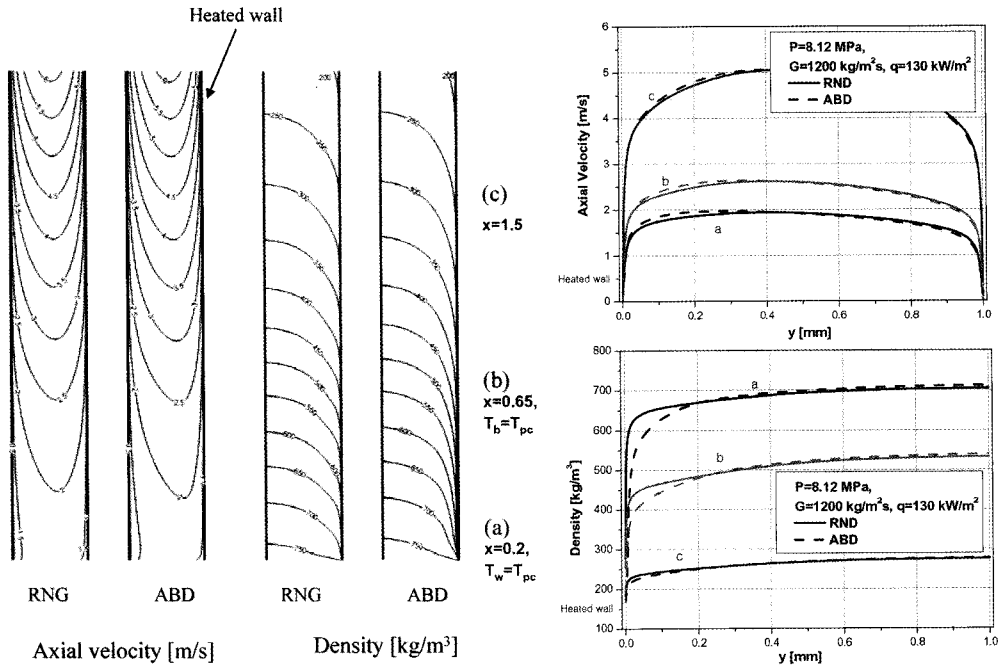

Fig. 12. Contour Plots and Comparison of the Predicted Axial Velocity and Density Profiles at the Radial Coordinates for the 8/10 mm Annular Channel (q=130 kW/m^2)

and this peak becomes lower with an increase of the heat flux. In this region we also noticed some remarkable differences in the heat transfer coefficient between the prediction and the measurement, which may have resulted from a measurement uncertainty of the temperature. The RNG model over-predicts the heat transfer coefficient throughout the entire heated length as this model predicts the turbulence near the wall higher than the other two models.

Figs. 9-12 show the contours and the distributions of the temperature, specific heat, axial velocity and density calculated by the two models for the cases of a heat flux of 50 and 130 kW/m^2, respectively. These physical property profiles are very similar to that of the tube, but the velocity profiles are rather different from those of the tube.

3.4 Heat Transfer Mechanism

To study the heat transfer mechanism at a region near the heated wall, the cross-sectional mean stream-wise velocity, temperature distributions, and turbulence kinetic energy were compared between the models for the case of a 130 kW/m^2 heat flux. The profiles of the normalized mean stream-wise velocity are given by wall coordinates (indicated by the '+' superscripts for y and u) as

$$u^+ = \frac{u}{u_\tau},\quad u_\tau = \sqrt{\frac{\tau_w}{\rho_w}},\quad y^+ = \frac{\rho_w u_\tau (R-r)}{\mu_w}, \tag{14}$$

and the normalized mean temperature difference is given by the wall coordinates as

$$\theta^+ = \frac{T-T_w}{T_\tau},\quad T_\tau = \frac{q_w}{\rho_w c_p u_\tau} \tag{15}$$

The distributions of $<u^+>$, $<\theta^+>$, and $<k/u_c^2>$ of the 4.4 mm tube for an enthalpy of 320 kJ/kg (a point of near the pseudo-critical condition indicated by A in Fig. 3) and 420 kJ/kg (a point of higher enthalpy downstream of the pseudo-critical point indicated by B in Fig. 3) are shown in Fig. 13. For the flow near the pseudo-critical point (point A), where a rapid change of the fluid properties occurs, the variation of the temperature (θ^+) is very large. But at a higher enthalpy region downstream of the pseudo-critical point (point B), where the variation of the fluid properties decreases, the temperature (θ^+) is also decreases. The near wall velocity (u^+) and turbulence kinetic energy normalized by the velocity at the center (k/u_c^2) also show a large variations at point A where a rapid change of the fluid properties occurs. At a higher enthalpy region downstream of the pseudo-critical point (point B), the variation of the velocity (u^+) near the wall is fitted very well to the correlation for the law of the wall. The RNG model underestimates the wall temperature (θ^+), while the SST and ABD models overestimate them. On the other hand, the SST and ABD models underestimate $<k/u_c^2>$.

The distributions of $<u^+>$, $<\theta^+>$and $<k/u_c^2>$ in the 8/10

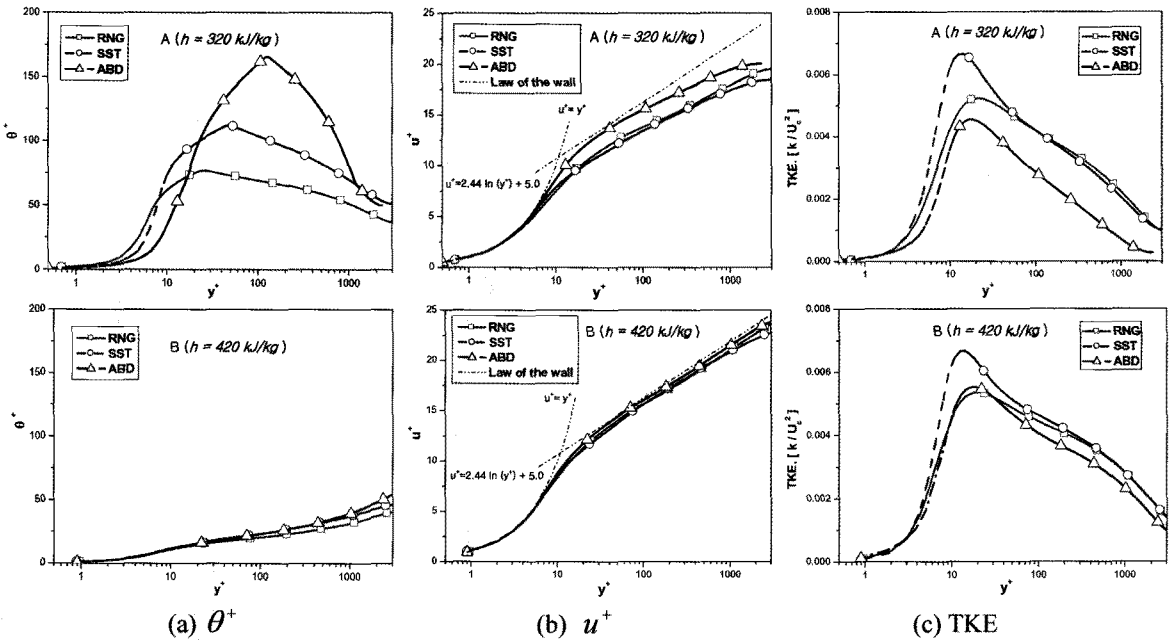

(a) θ^+ (b) u^+ (c) TKE

Fig. 13. Comparison of a) Predicted Mean Temperature Profiles in the Wall Coordinates, b) Predicted Stream-wise Mean Velocity Profiles, and c) Predicted Turbulent Kinetic Energy for the 4.4 mm Tube (q=130 kW/m^2)

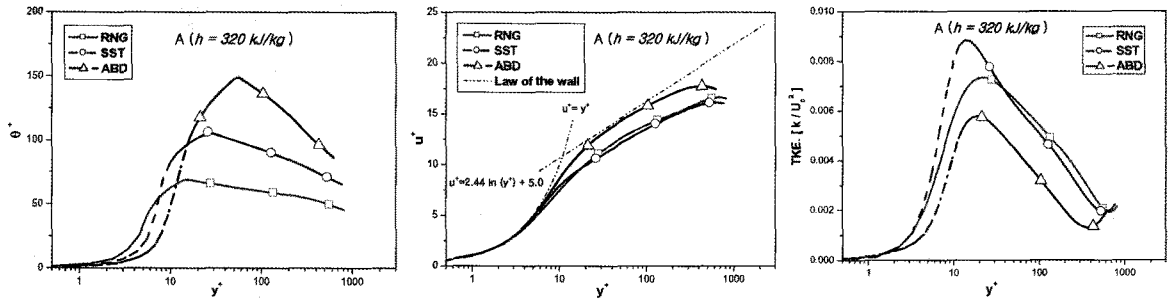

(a) θ^+ (b) u^+ (c) TKE

Fig. 14. Comparison of a) Predicted Mean Temperature Profiles in the Wall Coordinates, b) Predicted Stream-wise Mean Velocity Profiles, and c) Predicted Turbulent Kinetic Energy for the 8/10 mm Annular Channel (q=130 kW/m^2)

mm annular channel for an enthalpy of 320 kJ/kg (a point near the pseudo-critical condition indicated by A in Fig. 8) are shown in Fig. 14. The near wall velocity (u^+) characteristics for the annular channel are almost the same as the tube case, and the turbulence kinetic energy and the normalized temperature for the annular channel are also very similar to those for the tube. In the annular channel, as the flow passage (the distance from the flow center to the wall) is very small, the velocity gradient at the wall region is much higher than that in the tube even though u^+ in the annular channel shows almost the same distribution. The flow condition for the annular channel is similar to the case with the higher Reynolds number in the tube; the absolute value of the turbulence kinetic energy and the normalized temperature for an annular channel is larger than the tube case. Accordingly, even though the tendency is similar, the heat transfer coefficient increases on a similar scale for all the turbulence models.

3.5 Buoyancy Effects

One interesting factor that influences the flow at a supercritical pressure is the buoyancy effect. In the

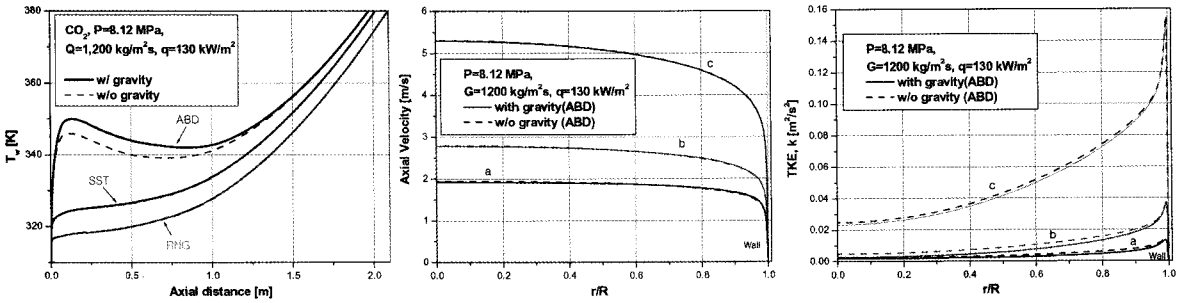

(a) T_w (b) Axial velocity (c) Turbulent kinetic energty

Fig. 15. Comparison of the Buoyancy Effect on the Turbulence Models for the 4.4 mm Tube

simulation of a supercritical pressure flow, a density change is considered directly in the form of conservation equations. But in the turbulence kinetic energy transfer equation as shown in Equation (6), the generation term due to the buoyancy effect is included as follows.

$$G_b = g_i \beta \overline{u_i' T'} = \beta g_i \frac{\mu_t}{\Pr_t} \frac{\partial T}{\partial x_i} \tag{16}$$

The above term decreases the turbulence kinetic energy when the temperature field is stable, i.e., a hot fluid is located of an upper location of the flow path. But if the temperature field is unstable, the term increases the turbulence kinetic energy. In the present simulation of vertical upward flow in a heated tube, the wall temperature continuously increases and the turbulence kinetic energy decreases. Fig. 15 shows the buoyancy effect very well. The buoyancy effects according to the turbulence models for the heat transfer of a 4.4 mm tube are compared. It can be seen that the buoyancy effect is more remarkable for the ABD than for the other two models. The temperature and axial velocity, predicted by the ABD model, are also plotted by calculating the heat transfer of the tube with and without a gravity term in Fig. 15 (a) and (b).

In general, the flow near the pseudo-critical point is highly susceptible to the effect of a rapid acceleration and the buoyancy effect when a strong wall heat flux is applied. In the heat transfer deterioration region, the ABD model may be a good candidate for a more accurate prediction of the flow and thermal fields although some additional modifications are still needed for a better prediction.

4. CONCLUSIONS

The thermal and flow fields of upward flowing CO_2 in a tube and an annular channel were simulated numerically by using the CFD code, Fluent 6.3. Three kinds of embedded turbulence models were examined by comparing the numerical simulation results with the experimental data. By comparing the calculation results for a tube and an annular channel, the effects of the selected geometries were examined as well. Some findings of the present work can be summarized as follows:

The predicted heat transfer coefficient for the annular channel is larger than that for the tube. The RNG model shows an over-prediction of the heat transfer coefficient than the SST and ABD models and the trend is similar for both geometries.

When the numerical predictions of a local heat transfer coefficient were compared with measurement results, the RNG model is better for the tube case, but the SST and ABD models are better for the annular channel. However, the experimentally obtained heat transfer coefficient with the same heat loading factor for both geometries showed similar profiles, so it is very difficult to say which model is better for the prediction.

The near wall velocity, the turbulence kinetic energy and the normalized temperature characteristics for the two geometries are almost the same. Even though the non-dimensional velocity shows almost the same, i.e., the flow condition is similar, the absolute value of turbulence kinetic energy and normalized temperature for the annular channel is larger than the tube case. Accordingly, the heat transfer coefficient for the annular channel increases on a similar scale for all the models.

The buoyancy effect is more remarkable for the ABD than for the other two models. Therefore the ABD model may be a good candidate for a more accurate prediction of the flow and thermal fields although some additional modifications are still needed for a better prediction.

ACKNOWLEDGMENTS

The authors would like to acknowledge the financial support of the Korea Atomic Energy Research Institute and the Ministry of Education, Science and Technology (MEST).

REFERENCES

[1] Y. Y. Bae, J. Jang, H. Y. Kim, H. O. Kang, and K. M. Bae, "Research activities on a supercritical pressure water reactor in Korea," *Nuclear Engineering and Technology*, Vol. 39, No. 4, pp. 273-286, August (2007)

[2] H. Y. Kim, H. Kim, J. H. Song, B. H. Cho, and Y. Y. Bae, "Heat transfer test in a vertical tube using CO_2 at supercritical pressures," *Journal of Nuclear Science and Technology*, Vol. 44, No. 3, pp. 283-293 (2007)

[3] S. H. Kim, Y. I. Kim, Y. Y. Bae, and B. H. Cho, "Numerical simulation of a vertical upward flow of water in a heated tube at supercritical pressure," *Proceeding of ICAPP'04*, Paper 4047, Pittsburgh, USA. (2004)

[4] S. Yoshida and H. Mori, "Heat transfer to supercritical fluids flowing in tubes," *Proc. of 1st Int. Symposium on Supercritical Water-Cooled Reactor Design and Technology (SCR-2000)*," pp. 72-78 , The University of Tokyo, Nov. 6-9 (2000)

[5] W. B. Hall and J. D. Jackson, "Laminarization of a turbulent pipe flow by buoyancy forces," ASME Paper No. 69-HT-55 (1969)

[6] E. W. Lemmon, M. O. McLinden, and M. L. Huber, NIST standard reference database 23, REFPROP Ver. 7.0 (2002)

[7] D. Choudhury, "Introduction to the renormalization group method and turbulence modeling," Fluent Inc. Technical Memorandum TM-107 (1993)

[8] F. R. Menter, "Two-equation eddy-viscosity turbulence models for engineering application," *AIAA Journal*, 32(8), pp. 1598-1605, August (1994)

[9] R. Abid, "Evaluation of two-equation turbulence models for predicting transitional flows," *Int. J. Engineering Science*, 31, pp. 831-840 (1993)

[10] Fluent Inc., "Fluent 6.3 User's Guide", Fluent Incorporated, Lebanon, NH (2006)

[11] M. Wolfstein, "The velocity and temperature distribution of one-dimensional flow with turbulence augmentation and pressure gradient," *Int. J. Heat Mass Transfer*, 12: pp.301-318 (1969)

[12] H. C. Chen and V. C. Patel. "Near-Wall Turbulence Models for Complex Flows Including Separation", *AIAA Journal*, Vol. 26, pp. 641-648 (1988)

[13] T. Jongen, "Simulation and modeling of turbulent incompressible flows," PhD thesis, EPF Lausanne, Lausanne, Switzerland (1992)

[14] J. D. Jackson and W. B. Hall, "Forced convection heat transfer to fluids at supercritical pressure, in turbulent forced convection in channels and bundles, Vol. 2, Hemisphere, pp. 563-611 (1979)

[15] H. Kim, H. Y. Kim, J. H. Song, and Y. Y. Bae, "Heat transfer to supercritical pressure carbon dioxide flowing upward through tubes and a narrow annulus passage," *Progress in Nuclear Energy 50*, pp. 518-525 (2008)